Thermomechanical fatigue failure investigation on a single crystal nickel superalloy turbine blade

Rongqiao Wang, Kanghe Jiang, Fulei Jing, Dianyin Hu

Thermomechanical fatigue failure investigation on a single crystal nickel superalloy turbine blade

Rongqiao Wang [a,b,c], Kanghe Jiang [a], Fulei Jing [d], Dianyin Hu [a,b,c,*]

[a] *School of Energy and Power Engineering, Beihang University, Beijing 100191, China*
[b] *Collaborative Innovation Center of Advanced Aero-Engine, Beijing 100191, China*
[c] *Beijing Key Laboratory of Aero-Engine Structure and Strength, Beijing 100191, China*
[d] *AVIC Academy of Aeronautic Propulsion Technology, Beijing 101304, China*

A thermomechanical fatigue (TMF) test rig was developed consisting of the loading, heating, synchronizing, cooling and monitoring systems. Moreover, the specimen was particularly designed to provide adequate load-bearing capability at the blade tip in order to simulate the actual turbine blade loads in laboratory. TMF test on a single crystal nickel superalloy turbine blade was conducted. Then the specimen was segmented in a novel way to preserve the crack surface to investigate the TMF mechanism of the turbine blade. Visual examination together with the metallographic analysis indicated that the most severe TMF damage occurred at the pin-fin fillet on the suction side near the trailing edge. Furthermore, finite element simulation results were compared to the experiment, in which a viscoplastic constitutive model was employed.

1. Introduction

Single crystal nickel superalloys are widely used to manufacture turbine blades and vanes in gas turbine engines for their superior high temperature performance [1]. Turbine blades operating in engines are subjected to simultaneously occurring thermal loads caused by the high temperature gas, and mechanical loads induced by the centrifugal force [2]. Generally, failure due to the contribution of both thermal and mechanical loading is termed thermomechanical fatigue (TMF), which is a major life-limiting factor for gas turbine blades [3–5]. Therefore the investigation on the TMF failure is of special interest in the gas turbine industry.

Over a period of years, experiments on standard specimens, such as round bars, are extensively conducted to investigate the material's deformation behavior and damage mechanisms under TMF loading [6–8]. Through these fruitful experiments, a wide variety of models involving constitutive equations for single crystal superalloy and TMF damage models has been established. These experiments facilitated the understanding of the TMF damage mechanism of the single crystal nickel superalloy material instead of the turbine blade, which laid a foundation for lifetime prediction. However, a sophisticated cooling scheme including intricately designed channels, film-cooling holes and pin-fins is widely used in modern advanced turbine blades in order to achieve the required lifetime, which results in extremely non-uniform stress/temperature fields under the service condition [4]. In addition, actual single crystal nickel based turbine blades are manufactured by investment casting [1], which is remarkably different from standard specimens fabricated by machining methods like turning, milling, grinding and polishing. These differences may cause discrepancies between their mechanical performance and life distribution [9].
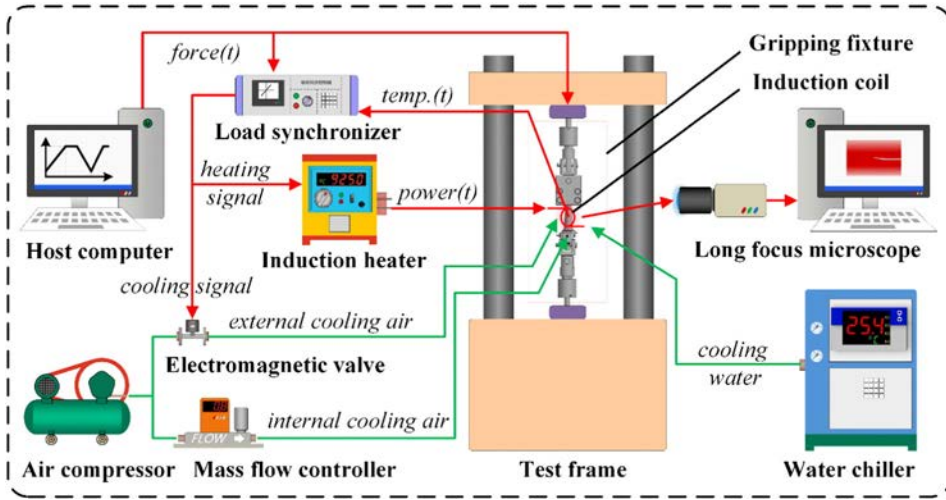
Fig. 1. The turbine blade TMF test system. (For interpretation of the references to color in this figure, the reader is referred to the web version of this article.)

It is known that performing aeroengine test under service condition to investigate turbine blades' failure is nearly impossible due to extremely high cost and difficulties in measuring turbine blades' temperature and stress fields. Consequently, the development of TMF experimental methods for actual turbine blades in lab is of great importance [10]. More recently, lots of experiments on the blade-like specimens and full scale blades have been carried out to meet the industrial requirements [5,10–14]. Especially the experiments on actual turbine blades help to investigate their failure mechanism in an affordable way. Additionally, experimental results can modify the developed models based on the standard specimen experimental data.

In this regard, the objective of this paper is to provide an effective method to investigate the turbine blade's TMF failure. A TMF test rig on actual turbine blades was constructed. Then a particularly designed specimen was tested under the TMF loading. The tested specimen was preliminarily inspected by an analytic scanning electron microscopy (SEM), and then segmented into metallographic samples through a new method to observe the crack surface directly. Visual examination and SEM inspection were performed on the samples to identify the TMF mechanism of the turbine blade by detailed microstructural characterization referred to [15,16]. In addition, finite element simulation based on a viscoplastic constitutive model was also conducted to validate the location where most sever TMF damage manifested.

2. Experimental details

2.1. Experimental set-up

Fig. 1 illustrated the TMF experiment system for the turbine blade, which consisted of a servo-hydraulic testing machine, a set of gripping fixture, a high frequency induction heater, an induction coil, a load synchronizer, a long-focus microscope, and the air/
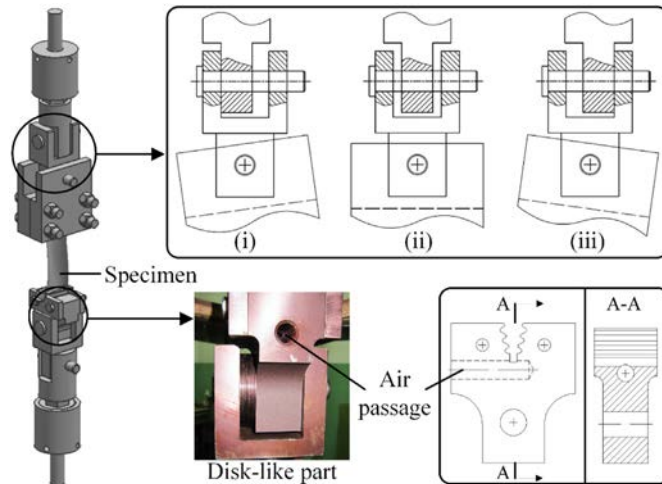

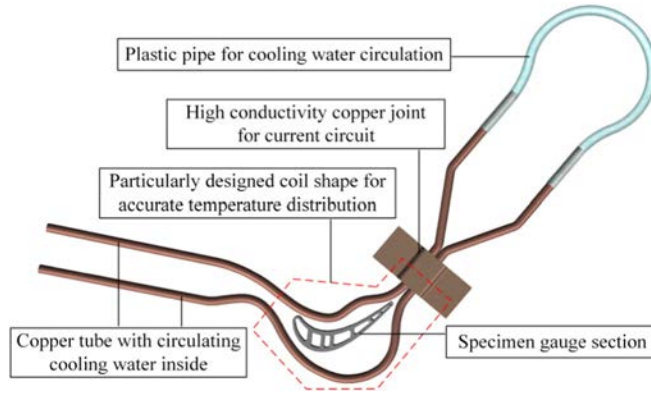**Fig. 2.** Gripping fixture schematic diagram.

Fig. 3. Internal water-cooled copper induction coil.

water cooling devices. The red lines represented signal paths for controlling or data acquisition, the green lines indicated the air/water cooling path. Some details were given as follows.

Loading system: The mechanical load was imposed by a fully computer-controlled servo-hydraulic testing machine of ± 50 kN capacity. Nevertheless, the testing machine could only generate uniaxial tension/compression load, which was unable to simulate the desired complex stress field in the gauge section of the turbine blade. To address this issue, a particular set of gripping fixture (Fig. 2) was designed to provide additional bending moment, which results in a complex stress field. In addition, an internal cooling passage within the disk-like part was designed to cool the specimen during the test. The detail adjustment procedure can be seen in [5].

Heating system: High frequency induction heating is an effective method to heat metallic materials due to its prominent advantages compared with other heating methods such as gas flow heating [10], radiation heating [17], i.e., it's very convenient to obtain the desired temperature field by adjusting the shape and size of the induction coil. Additionally, a sufficiently high heating rate can be obtained by increasing the heating power. Therefore, an induction heater combined with a water-cooled copper induction coil (Fig. 3) was utilized to heat the specimen.

Load synchronizing system: The phase angle between the thermal and mechanical loads is usually invariant in the TMF test, which means that thermal load and mechanical load change synchronously. Therefore, a load synchronizer was employed to maintain a stable phase shift. As shown in Fig. 1, the load synchronizer calculated the target temperature according to the force signal sent by the host computer. Meanwhile, the real-time temperature signal from a K-type thermocouple attached to the specimen was inputted into the load synchronizer. In light of the difference between the calculated target temperature and the real-time measured temperature, the load synchronizer would output heating/cooling signal to heat/cool the specimen. The heating signal would instruct the induction heater to work in proper heating power, while the cooling signal would change the on-off frequency of the normally closed electromagnetic valve. In this way, the specimen temperature field was precisely controlled.

Air cooling system: In order to implement the internal air cooling, an air compressor was utilized to provide compressed air. In addition, a mass flow controller was employed to precisely control the internal cooling air mass flow rate. Meanwhile, the external air cooling was performed through the close cooperation of the compressor, the electromagnetic valve and a nozzle straight pointed to the specimen. The external cooling capacity was accurately regulated by the electromagnetic valve, which was controlled by the cooling signal.

Crack monitoring system: In practice, the crack initiation will significantly change the temperature state at elevated temperature [10]. When a crack manifests on the specimen surface, the crack behaves like a dark line surrounded by the bright high temperature area. So clear is the brightness distinction that the crack can be easily detected. A Questar long-focus microscope with a 2 μm resolution was utilized to monitor the fatigue crack in real-time. The experiment continues till a visible crack is observed.

2.2. Material and specimen

The specimen was made of single crystal nickel-based superalloy DD6 in Chinese series (similar to Rene N5, PWA1484 and CMSX-4). The turbine blade was solution heat treated at 1290 °C and held for 1 h. Following the solution heat treatment, the turbine blade underwent heat treatments at 1300 °C for 2 h and 1315 °C for 4 h, after which it was air cooled to room temperature.

Table 1
Chemical composition of DD6 (wt%).

Ni	Al	Ta	W	Co	Re	Hf	Cr	Mo
Balance	5.2–6.2	6.0–8.5	7.0–9.0	8.5–9.5	1.6–2.4	0.05–0.15	3.8–4.8	1.5–2.5

Table 2
Mechanical properties for DD6 superalloy in the casting growth direction.

Temperature(°C)	25	700	760	850	980	1070
Elastic modulus (GPa)	131.5	107	105.5	98	80.5	69.5
Yield stress (MPa)	930	930	935	1030	680	440
Poisson's ratio	0.344	0.374	0.377	0.383	0.390	0.399

Then the turbine blade was heated to 1120 °C for 4 h followed by an air cool. Finally, the turbine blade was heated to 870 °C for 32 h, followed by an air cool. After the heat treatment, the material exhibits a two phase microstructure, with coherent and cuboidal γ′-precipitates that embedded in the γ matrix. The superalloy has a γ′ particle size of 300–500 nm and a γ′ volume fraction of approximately 65%. The material chemical composition (in wt%) was listed in Table 1.

Mechanical properties for DD6 superalloy at different temperatures are shown in Table 2.

The blade, which was in design phase, was a high pressure turbine blade with no shroud at the tip of the blade. However, in order to transmit the force from the gripping fixture, a handle was needed at the tip of the blade. Proceeding research showed that the blade with a shroud welded to the tip was not strong enough to withstand the cyclic mechanical load due to the weak weld joint strength. This was because the single crystal structure at the blade tip was destroyed owing to the welding process, which directly led to serious material performance degradation. Therefore, how to maintain the material performance at the connection was a fundamental issue to the experiment.

To solve this problem, a new approach was proposed in this research to provide adequate strength at the blade tip. Single crystal nickel turbine blades are manufactured by investment casting. Wax models are essentials to cast turbine blades [1]. In order to cast a shroud at the blade tip, a particularly designed shroud wax model (Fig. 4 (a)) was designed and manufactured. Then a new wax model was produced by assembling the original blade wax model (Fig. 4 (b)) with the shroud wax model, shown in Fig. 4 (c). With the new wax model, the specimen was cast as a whole in order to remain the single crystal structure. Therefore the blade-shroud connection could be able to inhibit unexpected fatigue crack nucleation nearby.

2.3. Experimental load conditions

As illustrated in Fig. 5, the test section was chosen where the maximum operational temperature occurred. The maximum temperature and stress values at representative positions for the test blade's section under service conditions were shown in Fig. 5.

The tested blade section was subjected to the cyclic thermal/mechanical loading. The experiment was conducted under load control with a stress ratio $R = 0.05$, equal to the ratio of the minimum load to the maximum load. The waveform of the TMF loading was represented by a trapezoidal stress/temperature wave with 35 s rise/heating, followed by 20 s dwell at the maximum load/temperature, and 25 s fall/cooling, as shown in Fig. 6. The minimum temperature in the thermal cycle was 200 °C.
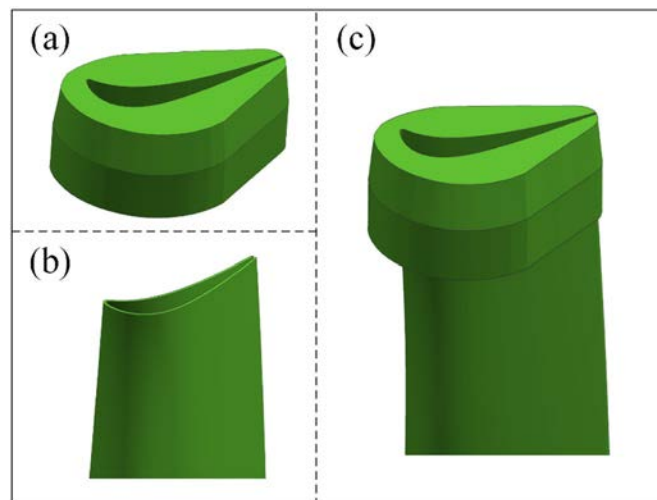

Fig. 4. Specimen wax model scheme: (a) shroud wax model; (b) original turbine blade wax model; (c) specimen wax model.
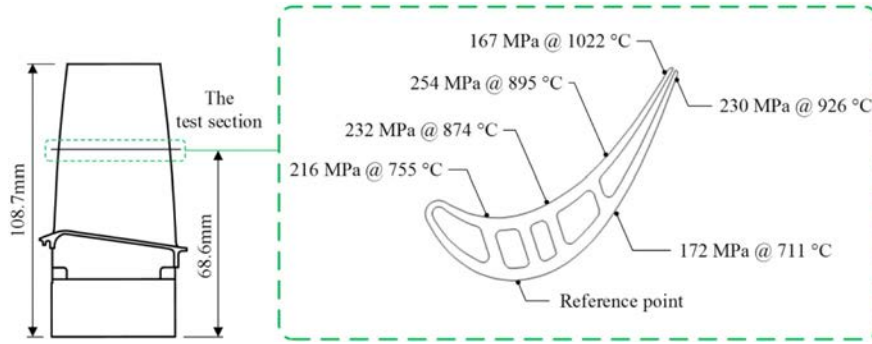
Fig. 5. The location of the test section and the maximum temperature/stress at representative positions of the test section.

3. Results and discussions

3.1. Preliminary inspection

The experiment was terminated after 325 cycles when a crack emerged at the suction side near the trailing edge. There were no visible cracks observed at other locations, especially in the vicinity of the film-cooling holes and the blade-shroud connection. No failure occurred for the test rig during the experiment, which verified the TMF experimental system was robust and reliable.

The specimen was preliminarily inspected by SEM to observe the crack morphology and also to find if there were other cracks that could not be seen with the naked eye. As can be seen in Fig. 7, the crack on the suction side was almost perpendicular to the loading direction.

Meanwhile, the other regions of the specimen were also inspected using the SEM, such as the film-cooling holes and other possible crack initiation sites. It turned out that there were no cracks at the film-cooling holes (Fig. 8) or other locations. This result demonstrated that TMF damage at film-cooling holes was not as severe as the pin-fin fillet for this blade. Therefore, major attention was focused on the observed crack. To learn more about the fatigue mechanism, more information should be obtained from the crack surfaces, which were still invisible in the suction side wall.

3.2. Metallographic sample preparation

The crack surfaces were expected to be well preserved on the metallographic samples for further inspection. Nevertheless, when the experiment was terminated the crack surfaces remained hidden in the blade suction side wall. To address this issue, the sample preparation method was developed to make metallographic samples with well-preserved crack surfaces. The detail steps taken were as follows (Fig. 9).

Step 1. The tested specimen was incised by a wire electrical discharge machine (WEDM) along the gauge cross section from leading edge to trailing edge. The incising process continued until the last about 15 mm (this length did not necessary to be accurate) was left (Fig. 9 (b)). It was worth reminding that the crack should be carefully protected from the WEDM. This was the reason why 15 mm length was remained uncut. This step significantly reduced the tensile force needed in Step 2. Additionally, it helped to separate the crack surfaces.
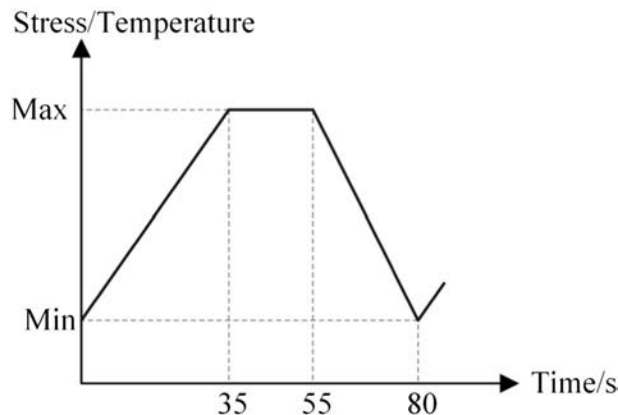
Fig. 6. Loading waveform for the TMF test.
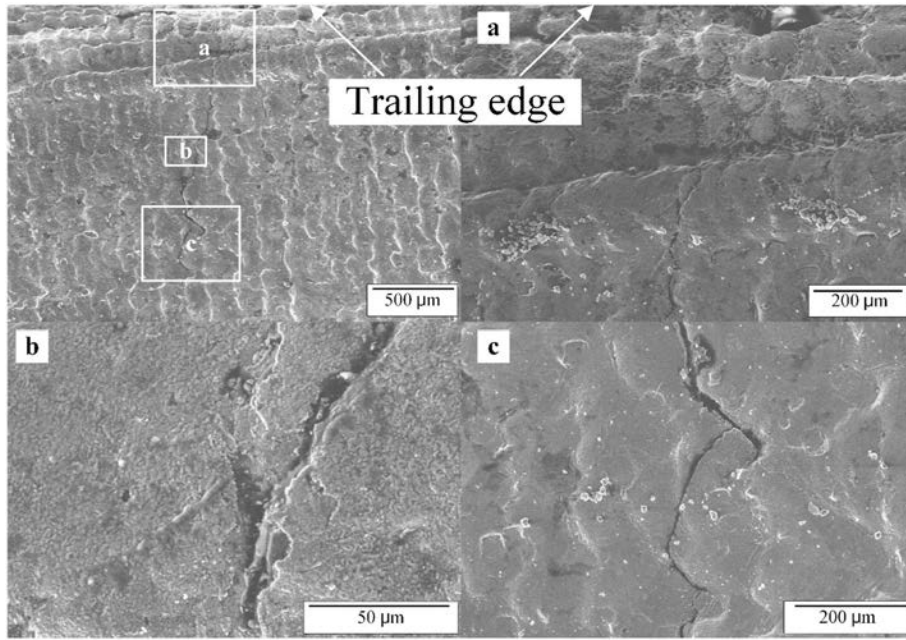
Fig. 7. The crack morphology: (a)–(c): higher magnification of the crack at different sites.

Step 2. The incised specimen was then mounted to the gripping fixture and loaded into the servo-hydraulic test machine. The test machine was set to the tension mode with a relatively slow speed. Gradually the specimen was pulled open (Fig. 9 (c)) and then split in half (Fig. 9 (d)). Finally 2 crack surfaces were preserved on each of them.

Step 3. Each specimen piece was then mounted into the WEDM again. Two small slices (Fig. 9 (e)) contained the crack surfaces were cut out from each specimen piece. In this way, the crack surfaces were well preserved on each sample, and hence could be observed directly.

3.3. Visual examination

Two samples were visually examined before metallographic inspection. Take sample 1 as an example, as shown in Fig. 10, there were 3 well defined regions on the sample. Region #1 was the wire cut area covered by wire cut marks. Region #2

Fig. 8. SEM photo of a film-cooling hole of the specimen.
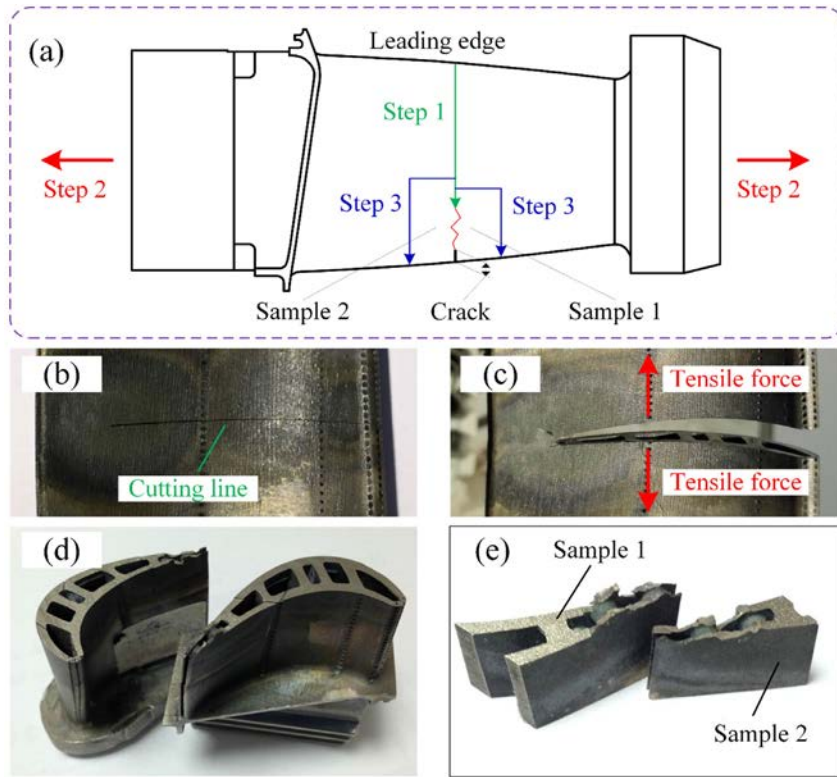
Fig. 9. Sample preparation procedures: (a) the overall procedure illustration; (b) the incised specimen; (c) the incised specimen was pulled open by the test machine; (d) the specimen was separated with crack surface preserved; (e) the prepared samples.

comprised lots of smooth glossy sharp planes. No signs of oxidation were observed on these planes. Their appearances presented cleavage fracture features. This was a matter of course since region #2 was generated by pulling the specimen in ha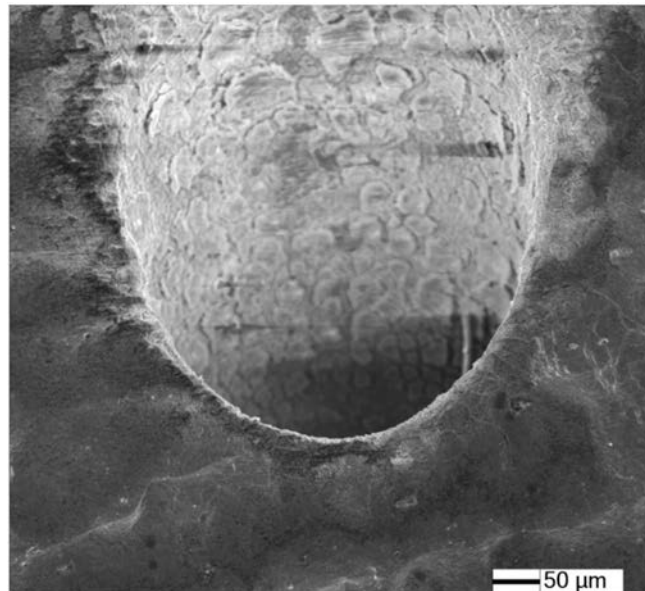lf during the 2nd step of sample preparation. Region #3 was the well-preserved crack surface, which was rough and dark, showing the sign of oxidation. This phenomenon proved that the sample preparation process was effective. Naturally, 3 corresponding regions (marked as region #1′, #2′ and #3′) existed on sample 2. The visual examination helped locate the approximate failure area, which would be intensively inspected by SEM to obtain more information.

3.4. Metallographic inspection

Sample 1 was inspected under low magnification in the first place. Multiple same scale images that focused on different sites were captured and then combined into a complete picture of the crack surface (Fig. 11). As shown in Fig. 11, the fracture surface in region #2 consisted of many smooth crystallographic planes. This result was consistent with the visual examination.

Most area of the crack surface was covered by oxidation layer. Oxidation played an important role during the crack propagation. However, fatigue features haven't been completely covered. Fatigue striations at spot A in Fig. 11 can be seen in Fig. 12. From

Fig. 10. Visual examination on sample 1.

Fig. 11. SEM photo of the crack surface on the suction side of sample 1.

the fatigue striation orientation, it was reasonable to postulate that the crack initiated at the pin-fin fillet, and propagated from the inside wall towards the outside.
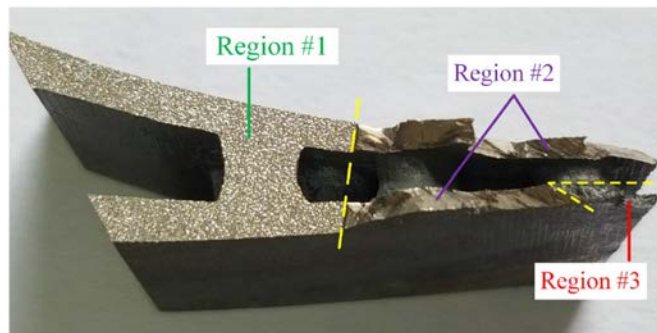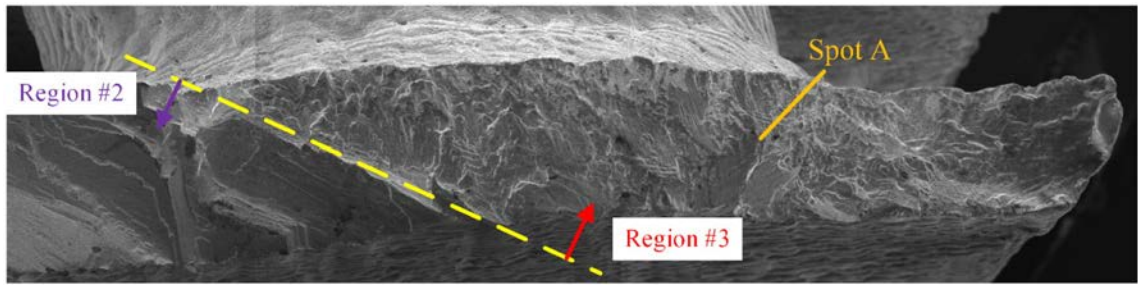
The other crack surface on sample 2 was also inspected. The complete picture of the crack surface (Fig. 13) was also formed by multiple same scale SEM image. Just like sample 1, most area of the crack surface was covered by uneven oxidation layer, which was dark and rough. The whole crack surface was intensively inspected, especially the area near the pin-fin. Some interesting results were presented in the high magnification picture (Fig. 14).

As shown in Fig. 14, the crack surface near the inside wall was severely oxidized. Some oxidation layer on the crack surface had even peeled off. The oxidation layer became thinner when closer to the outside wall. During fatigue experiment, new crack surface was less exposed to the elevated atmosphere than the crack surface generated earlier. Thus the difference in oxidation layer thickness indicated that the crack propagated from inside to outside. As the oxidation layer became thinner, the fatigue striations began to emerge. Beside this, the fatigue striations' density increased when near the inside wall. This phenomenon demonstrated that the crack propagated from the inside to the outside. Though the crack source could not be observed directly because of the thick oxidation layer, there were high chances that the crack initiated at the pin-fin fillet, according to the fatigue striations orientation. On the other hand, the role that stress concentration played here could not be neglected, since fatigue crack tended to initiate at the stress concentration zone [18].

No obvious fatigue striation was found at the crack surface during the early propagation stage. Thus we focused on the observed fatigue striations as shown in Fig. 14. The distance d from each fatigue striation to the inside wall was measured. The maximum distance $d_{max} = 425.7$ μm while the minimum distance $d_{min} = 281.9$ μm. Previous metallographic inspection results demonstrated that the crack propagated from the inside wall to the outside, so the scale of the crack size was in the same order as the wall thickness, and the crack size was less than the wall thickness, 574 μm. In this case, the Paris law was not suitable since it has been extensively applied for long crack. Instead, the crack propagation life was estimated by counting the striations in this study. Referred to [19–22], a one-to-one correspondence between striation and load cycle was claimed and well verified. Consequently, we assumed that each striation was induced by one load cycle. In this way, the evolution of distance d is shown in Fig. 15 (a).

It is revealed that the crack propagated rapidly at last several cycles, and soon the suction wall was penetrated. Until then, the crack propagated at a relatively steady growth rate. It's reasonable to assume a constant crack growth rate during the previous cycles. Based on this assumption, we straightly extended the curve in Fig. 15 (a) forward until it crossed the horizontal axis. As shown in Fig. 15 (b), the coordinate of the intersection point of the extension line (marked in green) and the horizontal axis is (261.3, 0), indicating that there are 50 striations covered by the thick oxidation layer. These striations, in addition to the observed ones, showed that there were 64 striations in total. So the crack propagation life was determined as 64 cycles, which accounted for 19.7% of the total fatigue life.
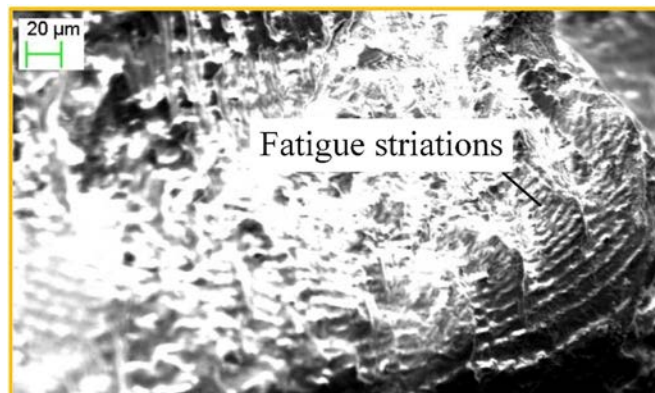
Fig. 12. Fatigue striations at spot A.
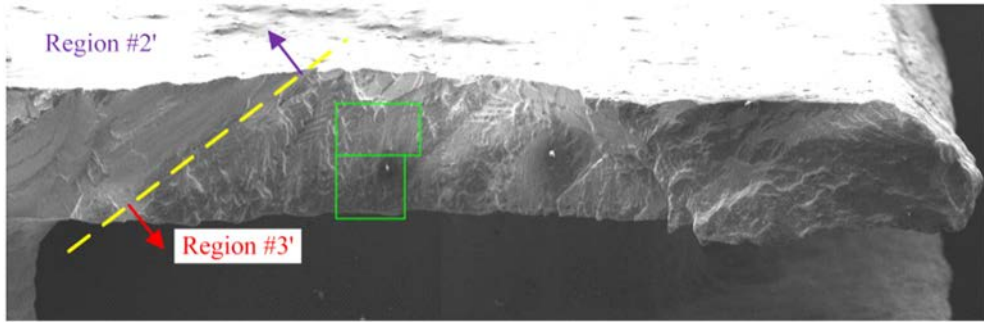
Fig. 13. SEM photo of crack surface on the suction side of sample 2.

4. Finite element simulation

Finite element simulation was carried out to study the specimen deformation behavior. The material's deformation was highly time-dependent when exposed to elevated temperature. This viscoplasticity was very much necessary to be described in material constitutive model. Therefore, a crystal plasticity based viscoplastic constitutive model, which was constructed by Walker [23] was chosen to calculate the high temperature deformation, especially the inelastic deformation. In this model, the total mechanical strain ε_m is divided into elastic strain ε_e and inelastic strain ε_{in}

$$\varepsilon_m = \varepsilon_e + \varepsilon_{in} \tag{1}$$

in which the inelastic strain includes the creep and plastic strains. The elastic strain is governed by generalized Hooke's law:

$$\sigma = C : \varepsilon_e \tag{2}$$

where σ is the macroscopic stress tensor and C is the stiffness tensor. While the inelastic strain is caused by the slip on 18 slip systems (12 octahedral slip systems {111} ⟨011⟩ and 6 cube slip systems {100} ⟨011⟩) of single crystal superalloy DD6. The well-known Schmid resolved shear stress π^r in the rth slip system is given by

$$\pi^r = \sigma : (\mathbf{m}^r \otimes \mathbf{n}^r) \tag{3}$$

Fig. 14. Local amplification SEM image of the crack surface on sample 2.

Fig. 15. Evolution of distance d: (a) the measured crack length at the range of 312–325 cycles; (b) the forward extended d vs. cycle. (For interpretation of the references to color in this figure, the reader is referred to the web version of this article.)

where $\mathbf{m}^r$ and n^r are the orientation tensors. The inelastic flow rule governing the slip rate $\dot{\gamma}^r$ in the rth slip system is:

$$\dot{\gamma}^r = \left|\frac{\pi^r - \omega^r}{K^r}\right|^{n-1}\left(\frac{\pi^r - \omega^r}{K^r}\right) \tag{4}$$

The back stress ω^r and the drag stress K^r are used to describe the kinematic hardening and isotropic hardening respectively. The evolution rule of ω^r and K^r can be seen in reference [23]. Material constants n may change with temperature under the cyclic thermomechanical loads. The 18 slip rates are then rotated from each slip system into crystallographic system. The relationship between the inelastic strain rate $\dot{\boldsymbol{\varepsilon}}_{in}$ and the slip rate is expressed as follows:
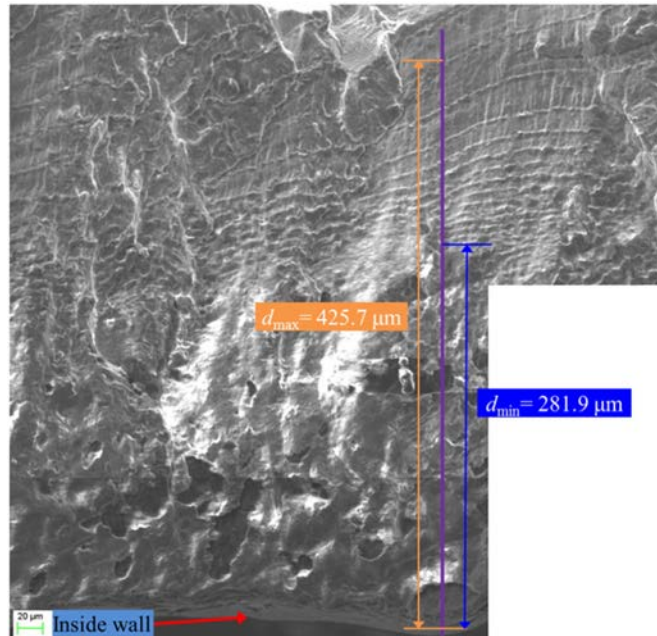
$$\dot{\boldsymbol{\varepsilon}}_{in} = \sum_{r=1}^{18} \dot{\gamma}^r (\mathbf{m}^r \otimes \mathbf{n}^r) \tag{5}$$

The inelastic strain increment is obtained by multiplying the inelastic strain rate by time increment. This constitutive model has been successfully applied to single crystal nickel superalloys such as PWA1480 and Hastelloy-X, and PWA1484 [23–27] due to the capability of simulating Baushinger effects, rate effects, stress relaxation and the remarkable history dependence of relaxation rates. Material parameters in the constitutive model for DD6 were identified by fitting the uniaxial standard specimen experimental data, as listed in Table 3. For simplicity, the detail meaning of each material constant could refer to reference [23]. Then the constitutive model was implemented using the material user routine *Hypela2* in the commercial finite element package MSC. Marc.

The constructed finite element model was shown in Fig. 16 (a). The elements near the pin-fin and film-cooling holes were carefully arranged in order to guarantee the simulation precision. The simulation was performed in 2 cycle periods. In this research, the TMF lifetime was remarkably lower than 50,000 cycles, thus the inelastic strain was supposed to be the primary concern. As stated before, the inelastic strain was due to the crystal slip, so the location with the maximum slip would be considered as the weakest point.

At the end of the simulation, most of the area presented near-zero accumulated slip. However a fair amount of slip emerged at the pin-fin fillet and the film-cooling holes. It's reasonable since the stress concentration effect played a significant role here. The accumulated slip distribution at the film-cooling hole, which presented the maximum accumulated slip among all of the film-cooling holes, and the pin-fin were shown in Fig. 16 (b) and Fig. 16 (c) respectively. Moreover, the maximum accumulated slip occurred at the pin-fin fillet with the accumulated slip was 6.5e−5, while the maximum accumulated slip at the edge of the film-cooling hole was 4.2e−5. This indicated that pin-fin fillet suffered more damage than the film-cooling holes since the maximum accumulated slip strain at the pin-fin fillet was 54.8% higher than the film-cooling holes, which resulted in shorter life at the pin-fin fillet. The simulation results demonstrated that the pin-fin fillet had the weakest TMF resistance, which was consistent with the experimental results.

Table 3
Material constants for the constitutive model of DD6 superalloy.

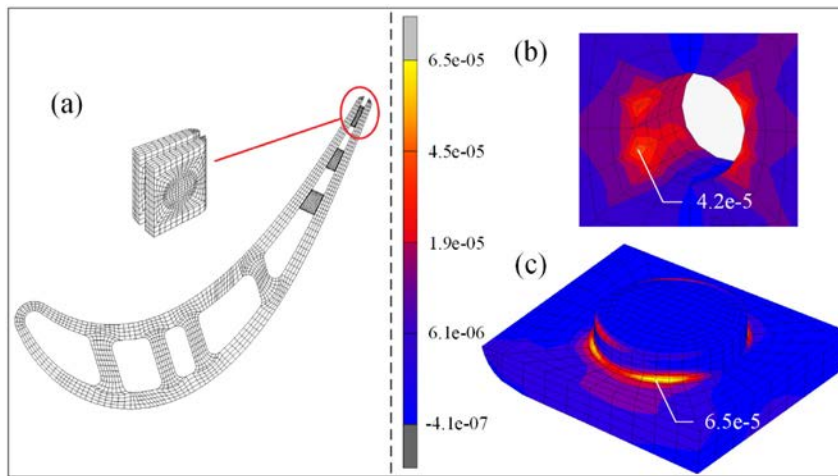| Material constants	ρ_1^ω	ρ_2^ω	ρ_4^ω	ρ_5^ω	K_0^ω	n	ρ_1^ς	ρ_2^ς	K_0^ς	m
760 °C	5.0e6	2.1e4	0.15	0.1	4.3e2	9.0	5.0e6	1.9e4	4.4e2	10.5
980 °C	2.0e6	0.374	0	−0.5	6.4e2	8.1	5.0e5	5.0e3	5.9e2	7.1
$\rho_3^\omega = \rho_3^\varsigma = \rho_4^\omega = \rho_5^\varsigma = 0$										

Fig. 16. Finite element simulation: (a) the finite element model; (b) accumulated slip distribution at a film-cooling hole; (c) accumulated slip distribution at the pin-fin.

5. Conclusions

Turbine blade TMF failure was investigated on the constructed TMF test rig. The sophisticated test rig consisted of loading, heating, synchronizing, cooling and monitoring systems proved to be reliable. No cracks initiated at the blade tip, the particularly designed specimen presented adequate load-bearing capability.

The prepared metallographic samples enabled direct inspection on the crack surfaces. Visual examination showed that the TMF failure occurred at the suction side near the trailing edge. Further metallography analysis revealed that the TMF crack initiated at the pin-fin fillet and propagated towards the outside wall.

Finite element simulation validated that the pin-fin fillet near the trailing edge suffered the most severe TMF damage. Measures should be taken to improve the TMF resistance at the pin-fin fillet, including, but not limited to, increasing the pin-fin fillet radius to reduce the stress concentration effect, and lowering the temperature nearby for better material durability.

Acknowledgements

References

[1] R.C. Reed, The Superalloys: Fundamentals and Applications, Cambridge University Press, New York, 2006.
[2] A. Pineau, S.D. Antolovich, High temperature fatigue of nickel-base superalloys – a review with special emphasis on deformation modes and oxidation, Engineering Failure Analysis. 16 (2009) 2668–2697.
[3] M. Segersäll, P. Kontis, S. Pedrazzini, P.A.J. Bagot, M.P. Moody, J.J. Moverare, et al., Thermal–mechanical fatigue behaviour of a new single crystal superalloy: effects of Si and Re alloying, Acta Materialia. 95 (2015) 456–467.
[4] R.K. Kersey, A. Staroselsky, D.C. Dudzinski, M. Genest, Thermomechanical fatigue crack growth from laser drilled holes in single crystal nickel based superalloy, International Journal of Fatigue. 55 (2013) 183–193.
[5] R. Wang, F. Jing, D. Hu, In-phase thermal–mechanical fatigue investigation on hollow single crystal turbine blades, Chinese Journal of Aeronautics. 26 (2013) 1409–1414.
[6] ISO, Metallic materials — Fatigue testing — Strain-controlled thermomechanical fatigue testing method, BSI Standards Publication, Switzerland, 2011.
[7] ASTM, Standard Practice for Strain Controlled Thermomechanical Fatigue Testing, 2010.
[8] P. Hähner, E. Affeldt, T. Beck, H. Klingelhöffer, M. Loveday, C. Rinaldi, Validated Code-of-practice for Strain-controlled Thermo-mechanical Fatigue Testing, 2006.
[9] D. Hu, R. Wang, Combined fatigue experiments on full scale turbine components, Aircraft Engineering and Aerospace Technology. 85 (2013) 4–9.
[10] N.G. Bychkov, V.P. Lukash, Y.A. Nozhnitsky, A.V. Perchin, A.D. Rekin, Investigations of thermomechanical fatigue for optimization of design and production process solutions for gas-turbine engine parts, International Journal of Fatigue. 30 (2008) 305–312.
[11] C. Charles, Multiaxial Testing of Gas Turbine Engine Blades, 36th AIAA/ASME/SAE/ASEE Joint Propulsion Conference and ExhibitAmerican Institute of Aeronautics and Astronautics 2000.
[12] O. Mallet, H. Kaguchi, B. Ilschner, F. Meyer-Olbersleben, K. Nikbin, F. Rézaï-Aria, et al., Influence of thermal boundary conditions on stress-strain distribution generated in blade-shaped samples, International Journal of Fatigue. 17 (1995) 129–134.
[13] M. Thiele, S. Weser, U. Gampe, R. Parchem, S. Forest, Advancement of experimental methods and cailletaud material model for life prediction of gas turbine blades exposed to combined cycle fatigue, ASME Turbo Expo 2012: Turbine Technical Conference and Exposition, Copenhagen, Denmark 2012, pp. 119–130.
[14] H. Wang, Test methods on thermal on thermal/mechanical fatigue (TMF) of turbine blade, Aeroengine. 33 (2007) 7–11.
[15] H.M. Tawancy, L.M. Al-Hadhrami. Comparative performance of turbine blades used in power generation: damage vs. microstructure and superalloy composition selected for the application. Engineering Failure Analysis. 46 (2014) 76–91.
[16] W. Maktouf, K. Saï, An investigation of premature failure failures of gas turbine blade, Engineering Failure Analysis. 47 (2015) 89–101.

[17] B. Baufeld, M. Bartsch, M. Heinzelmann, Advanced thermal gradient mechanical fatigue testing of CMSX-4 with an oxidation protection coating, International Journal of Fatigue. 30 (2008) 219–225.

[18] C. Liu, B. Zhang, S. Yang, Y. He, C. Tao, Analysis of fracture and cracks of single crystal blades in aero-engine, Engineering Failure Analysis. 18 (2011) 582–589.

[19] W.C. Connors, Fatigue striation spacing analysis, Materials Characterization. 33 (1994) 245–253.

[20] Z. Khan, A. Rauf, M. Yonas, Prediction of fatigue crack propagation life in notched members under variable amplitude loading, J Mater Eng Perform (USA) 6 (3) (1997) 365–373.

[21] E. Hershko, N. Mandelker, G. Gheorghiu, H. Sheinkopf, I. Cohen, O. Levy, Assessment of fatigue striation counting accuracy using high resolution scanning electron microscope, Engineering Failure Analysis. 15 (2008) 20–27.

[22] S.P. Lynch, Progression markings, striations, and crack-arrest markings on fracture surfaces, Materials Science and Engineering: A. 468–470 (2007) 74–80.

[23] E.H. Jordan, K.P. Walker, A viscoplastic model for single crystals, Journal of Engineering Materials and Technology. 114 (1992) 19–26.

[24] E.H. Jordan, S. Shi, K.P. Walker, The viscoplastic behavior of hastelloy-X single crystal, International Journal of Plasticity. 9 (1993) 119–139.

[25] K.P. Walker, E.H. Jordan, Biaxial constitutive modelling and testing of a single crystal superalloy at elevated temperature, in: M.W. Brown, K.J. Miller (Eds.), Biaxial and Multiaxial Fatigue, Mechanical Engineering Publications, London 1989, pp. 145–170.

[26] D.M. Nissley, T.G. Meyer, K.P. Walker, Life Prediction and Constitutive Models for Engine Hot Section Anisotropic Materials Program, NASA-CR-189223, 1992.

[27] J. Gallagher, T. Nicholas, A. Gunderson, et al., Advanced High Cycle Fatigue (HCF) Life Assurance Methodologies, AFRL-ML-WP-TR-2005-4102, 2004.